AIAA JOURNAL
Vol. 37, No. 5, May 1999

Unsteady-State Simulation of Model Ram Accelerator in Expansion Tube

Jeong-Yeol Choi*
Pusan National University, Pusan 609-735, Republic of Korea
and
In-Seuck Jeung† and Youngbin Yoon*
Seoul National University, Seoul 151-742, Republic of Korea

Steady- and unsteady-state numerical simulations have been carried out to investigate the ram accelerator flowfield that had been studied experimentally using an expansion tube facility at Stanford University. Navier–Stokes equations for chemically reactive flows were used for the modeling with a detailed hydrogen–air combustion mechanism. The governing equations were analyzed using a fully implicit and time-accurate total variation diminishing scheme. As a result, steady-state simulation reveals that the near-wall combustion regions are induced by aerodynamic heating in the separated flow region. This result agrees well with experiments in the case of the $2H_2 + O_2 + 17N_2$ mixture but fails to reproduce the centerline combustion in the case of the $2H_2 + O_2 + 12N_2$ mixture. To investigate the reason for this disagreement in the flow establishment process, unsteady-state simulations have been carried out, and the results show the detailed process of flow stabilization. The centerline combustion is revealed to be an intermediate process during flow stabilization. It is induced behind a Mach stem formed by the intersection of strong oblique shock waves at an early stage of the flow stabilization process. This primary combustion zone is sustained for 30 and 40 μs respective to the mixtures and completely disappears later. The overall time needed for flow stabilization is about 150 μs, and the steady-state result is recovered.

Introduction

A RAM accelerator is a mass launching device using the principle of ramjet propulsion as an acceleration mechanism of a projectile in a barrel.[1] In a ram accelerator, shock waves compress a combustible mixture gas, and thrust is generated by high-speed combustion mechanism, such as shock-induced combustion or oblique detonation. In addition to the concept of a high-speed firing system, the ram accelerator has gained public interest as a new space launching technology and a ground-based research model of a scramjet engine.[2] For the past decade, many experimental, theoretical, and computational studies have been devoted to its development, and several ram accelerator facilities have been constructed. Currently, a maximum velocity of 2.7 km/s has been reported,[3] even though the theoretical performance of the ram accelerator is more than 10 km/s (Ref. 1). One of the practical reasons for the velocity limit is a heat transfer problem, but a more basic problem is lack of awareness of combustion characteristics during the acceleration process. Actually, the combustion mechanism in the ram accelerator is not yet clearly understood in spite of the various computational and experimental studies.

In research of flow physics, visualization should be the first consideration for understanding the flowfield. Knowlen et al.[4] and Kruczynski et al.[5] presented a highly luminous combustion zone behind a projectile by direct photography of a ram accelerator flowfield using a thick transparent acrylic barrel. Sasoh et al.[6] showed the detailed process of a diaphragm rupturing without combustion using a specially fabricated optical barrel. However, detailed visualization data of the reactive flowfield are not yet available due to difficulties arising from high luminosity and short flight time. As an alternative to the direct visualization of the moving ram accelerator flowfield, Morris et al.[7] recently attempted the visualization of stationary ram accelerator flowfield using a model ram accelerator. An expansion tube facility, capable of accelerating combustible gases up to hypersonic velocity, was used to model the stationary ram accelerator flowfield. The visualization of the reactive flowfield was made possible using schlieren photography and a planar laser-induced fluorescence (PLIF) imaging technique. Although the experiment was carried out at very low pressure compared to the actual fill pressure of the ram accelerator, the experiment has importance for the visualization of reactive flow in the ram accelerator configuration in addition to the highly tuned visualization techniques. The result of Morris et al.[7] is considered to show the important combustion mechanisms in a ram accelerator, especially the viscous effects on the combustion revealed by previous computational studies.[8–10] Nevertheless, their results left some questions about the steadiness of the experiment and the differences between the experimental cases. Also, clear understanding of the detailed flow features needs more evidence than their images provided; hence, computational methods would aid in solving this problem.

A number of computational studies have been carried out previously, which presented important combustion physics in a ram accelerator such as the viscous effect, the flow establishment process, and the structure of oblique detonations.[8–13] They presented the highly resolved flowfield but lacked validation because the results were rarely compared with experimental results. The visualized flowfield data were not available from experiments for some cases, and other studies used ideal configurations that have not been used in experiments. This paper presents the steady- and unsteady-state computational simulations of the model ram accelerator flow studied experimentally by Morris et al.[7] The combustion mechanism in a ram accelerator is investigated by comparing the computational results with experimental images, and issues about the steadiness of the experiment and the difference between the experimental cases are discussed.

Governing Equations and Combustion Mechanism

For the simulation of the model ram accelerator in an expansion tube, coupled forms of species conservation equations and Navier–Stokes equations are employed to analyze the reactive viscous flow in two-dimensional coordinates. The conservation form

Received April 7, 1998; presented as Paper 98-3450 at the AIAA/ASME/SAE/ASEE 34th Joint Propulsion Conference, Cleveland, OH, July 13–15, 1998; revision received Dec. 11, 1998; accepted for publication Jan. 2, 1999. Copyright © 1999 by the authors. Published by the American Institute of Aeronautics and Astronautics, Inc., with permission.

*Assistant Professor, Department of Aerospace Engineering. Member AIAA.
†Professor, Department of Aerospace Engineering. Senior Member AIAA.

of the governing equations for N species is written in general curvilinear (ξ, η) coordinates:

$$\frac{1}{J}\frac{\partial \boldsymbol{Q}}{\partial t} + \frac{\partial \boldsymbol{F}}{\partial \xi} + \frac{\partial \boldsymbol{G}}{\partial \eta} = \frac{1}{J}\boldsymbol{W} + \frac{\partial \boldsymbol{F}_v}{\partial \xi} + \frac{\partial \boldsymbol{G}_v}{\partial \eta} \tag{1}$$

$$\boldsymbol{Q} = [\rho_k, \rho u, \rho v, e]^T, \qquad k = 1, \ldots, N_s \tag{2}$$

where $\boldsymbol{Q}$ is the vector of conservative variables; $\boldsymbol{F}$ and $\boldsymbol{G}$ are the convective flux vectors in the ξ and η directions, respectively; $\boldsymbol{F}_v$ and $\boldsymbol{G}_v$ are viscous flux vectors; and $\boldsymbol{W}$ is the reaction source vector. The total density ρ is expressed as a sum of the partial density ρ_k of each species over a number of species N_s. Also, u and v are velocity components in Cartesian coordinates (x, y), and the total energy per unit volume e is defined as a sum of kinetic energy and internal energy. J is the metric Jacobian obtained from a coordinate transform relation. Detailed descriptions of the vectors in Eq. (1) and additional state and constitutive equations are well documented in the literature.[10] The present hydrogen–oxygen–nitrogen combustion mechanism is obtained from a Jachimowski mechanism[14] by ignoring the nitrogen dissociation reactions that have negligible effect on flowfield characteristics. The combustion mechanism consists of 9 species and 19 reaction steps, which had been validated from the unsteady-state simulation of periodically oscillating shock-induced combustion by comparing the oscillation frequencies and the locations of shock and reaction front with experimental results.[15]

For the present simulation of the model combustor, the whole flowfield is assumed to be laminar. Even with the very high flow velocity, the Reynolds number based on the combustor length is about 1×10^6 due to the small size of the model. Even though shock wave/boundary-layer interaction could make the flow turbulent, there is no clear evidence of the importance of turbulence on the global combustion characteristics in this experiment. Therefore, the laminar assumption would be applicable in view of computational efficiency. Moreover, as was discussed previously,[10] there is no adequate turbulence model that can predict the interaction between the chemistry and turbulence in the region of strong shock wave/boundary-layer interaction.

Numerical Formulation

Equation (1) is discretized by a finite volume approach. The numerical schemes for the discretization are well documented in the references[10,15] and summarized here. The convective fluxes are formulated using Roe's flux difference splitting method[16] derived for multispecies reactive flow. A MUSCL-type variable extrapolation approach is used to get a high-order spatial accuracy, and a differentiable limiter is used to preserve the total variation diminishing property.[17] A central difference method is used for viscous fluxes. For the case of the steady-state solution, a first-order accurate implicit scheme is used for the temporal integration of the governing equations. A lower–upper (LU) relaxation scheme[18] is used for the implicit analysis with approximate splitting of the flux Jacobian matrix.

In the case of unsteady-state simulation, the second-order accurate implicit method is used for time integration. A Newton subiteration method is used to preserve the time accuracy and solution stability at a large time step:

$$\left[c_0\boldsymbol{I} - \left(\frac{\partial \boldsymbol{R}}{\partial \boldsymbol{Q}}\right)\right]^{n+1,m}_{i,j} \Delta\boldsymbol{Q}^{n+1,m}_{i,j} = -c_0\boldsymbol{Q}^{n+1,m}_{i,j} - c_1\boldsymbol{Q}^{n}_{i,j} - c_2\boldsymbol{Q}^{n-1}_{i,j} + c_0\boldsymbol{R}\left(\boldsymbol{Q}^{n+1,m}_{i,j}\right) \tag{3}$$

$$\boldsymbol{Q}^{n+1,m+1}_{i,j} = \boldsymbol{Q}^{n+1,m}_{i,j} + \Delta\boldsymbol{Q}^{n+1,m}_{i,j} \tag{4}$$

where $\boldsymbol{R}$ is residual vector consisting of spatially discretized flux and source vectors, n is the index of the time integration step, and m is the index of the subiteration step. The coefficients c_0, c_1, and c_2 are the functions of variable time step size from second-order temporal discretization.[15]

The implicit part of Eq. (3) is inverted by the following LU symmetric Gauss–Seidel sweeps at every subiteration level[15]:

$$\boldsymbol{D}_{i,j}\Delta\boldsymbol{Q}^{*}_{i,j} = \mathbf{RHS}_{i,j} + \boldsymbol{A}^{+}_{i-1,j}\Delta\boldsymbol{Q}^{*}_{i-1,j} + \boldsymbol{B}^{+}_{i,j-1}\Delta\boldsymbol{Q}^{*}_{i,j-1} \tag{5}$$

$$\boldsymbol{D}_{i,j}\left(\Delta\boldsymbol{Q}^{n+1,m}_{i,j} - \Delta\boldsymbol{Q}^{*}_{i,j}\right) = -\boldsymbol{A}^{-}_{i+1,j}\Delta\boldsymbol{Q}^{n+1,m}_{i+1,j} - \boldsymbol{B}^{-}_{i,j-1}\Delta\boldsymbol{Q}^{n+1,m}_{i,j-1}$$

where

$$\boldsymbol{D}_{i,j} = c_0\boldsymbol{I} + [(\boldsymbol{A}^{+} - \boldsymbol{A}^{-}) + (\boldsymbol{B}^{+} - \boldsymbol{B}^{-}) - \boldsymbol{Z}]_{i,j} \tag{6}$$

Here, **RHS** is a vector consisting of the terms in the right-hand side of Eq. (3). $\boldsymbol{A}^{\pm}$ and $\boldsymbol{B}^{\pm}$ are split flux Jacobian matrices of convective fluxes $\boldsymbol{F}$ and $\boldsymbol{G}$. Split flux Jacobian matrices are obtained by the Steger–Warming method.[17] $\boldsymbol{Z}$ is the Jacobian matrix of the chemical source term $\boldsymbol{W}$. The subtraction terms of the split Jacobian matrices in Eq. (6) are evaluated by a single formulation without the abundant evaluation of split Jacobian matrices and matrix subtraction. Also, the matrix vector product term $\boldsymbol{A}^{\pm}\Delta\boldsymbol{Q}$ on the right-hand side of Eq. (5) is evaluated in a compact vector formulation without the evaluation of a split Jacobian matrix and a matrix–vector product. This formulation is derived in a manner similar to Eq. (16) in Ref. 10, and details about the formulation are described in Ref. 15. The numerical methods used in this study have been validated by the steady- and unsteady-state simulation of periodically oscillating shock-induced combustion and other experimentally known phenomena.[10,15]

Model Geometry and Flow Conditions

Figure 1 is a schematic configuration of the model ram accelerator used in the experiment by Morris et al.[7] It was configured symmetrically on the lower and upper sides to eliminate the effect of the wall boundary layer that is very small in a real ram accelerator configuration. Because of this symmetric shape, the model looks very similar to the hollow projectile configurations that were used in the computational study by Thibault et al.[19] and in the experimental study by Sasoh et al.[20] The experiment had been performed for two different mixtures, $2H_2 + O_2 + 12N_2$ and $2H_2 + O_2 + 17N_2$, and the flow conditions of the test gases arriving at the model ram accelerator are listed in Table 1. The computational domain is also

Table 1 Experimental conditions of test gases at tube exit[7]

Case	$2H_2 + O_2 + 17N_2$	$2H_2 + O_2 + 12N_2$
M_∞	5.2	5.2
T_∞, K	350	350
p_∞, bar	0.112	0.112

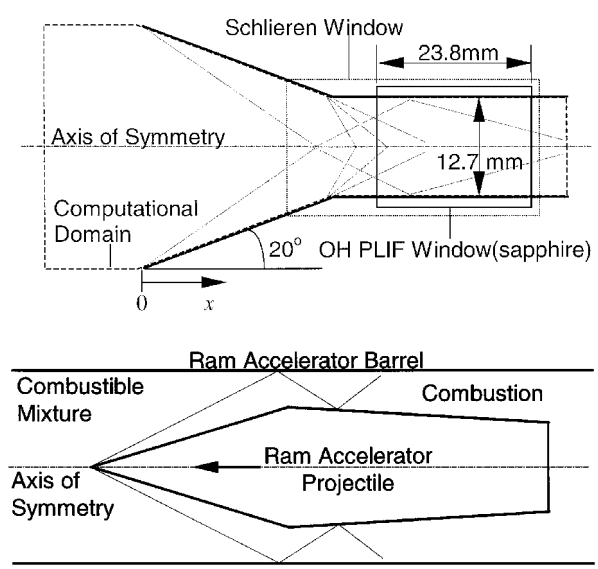

Fig. 1 Schematic of the configuration of model ram accelerator[7] compared with conventional ram accelerator geometry.

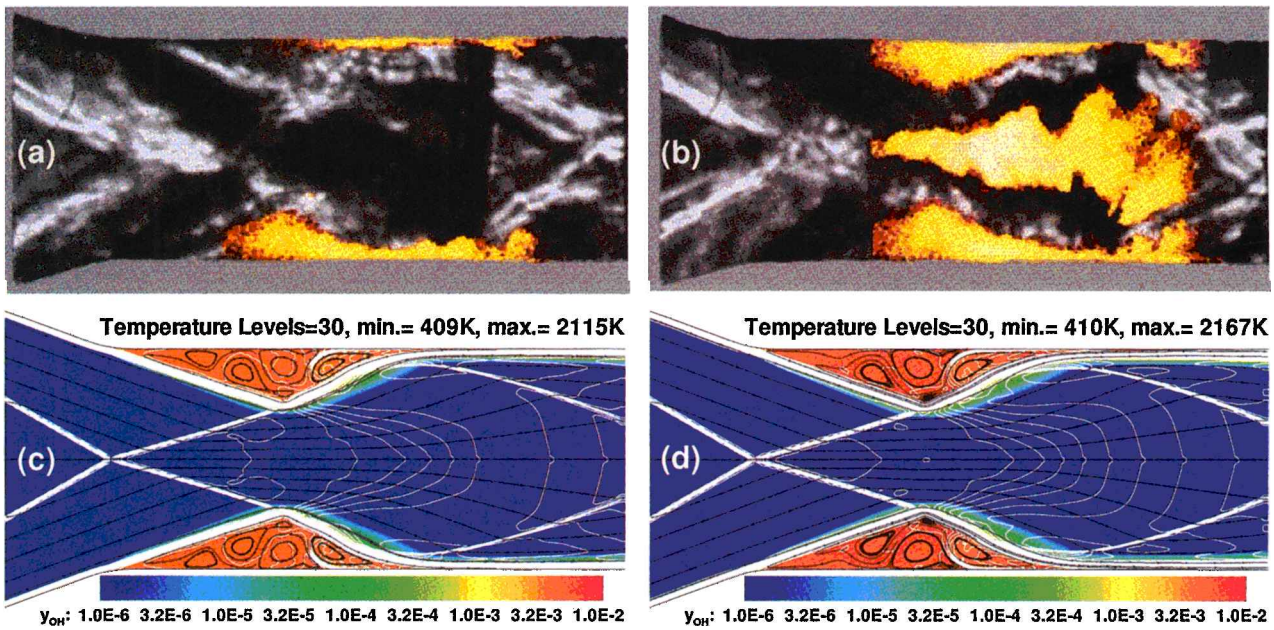

Fig. 2 Comparison of experimental results and numerical results with steady-state assumption (courtesy of Morris et al.[7] for the experimental results): a) overlaid schlieren and OH PLIF image for $2H_2 + O_2 + 17N_2$ mixture; b) overlaid schlieren and OH PLIF image for $2H_2 + O_2 + 12N_2$ mixture; c) overlaid OH mass fraction distribution, temperature contours, and streamlines for $2H_2 + O_2 + 17N_2$ mixture; and d) overlaid OH mass fraction distribution, temperature contours, and streamlines for $2H_2 + O_2 + 12N_2$ mixture.

shown in Fig. 1. The same computational domain is used for both steady- and unsteady-state computations, and it is extended in front of the model to include the wave interactions that may occur in the initial phase of the unsteady-state computation. The computational domain is covered by a 300×200 grid system, which is equally spaced in the flow direction and clustered to both walls. No-slip and adiabatic boundary conditions are applied at the body surfaces, and a supersonic boundary condition is applied at the exit. A grid refinement study has been performed for the $2H_2 + O_2 + 17N_2$ case with the steady-state assumption; 100×100, 170×120, 200×160, 300×200, and 400×250 grid systems have been tested; and wall pressure and shear stress distributions were compared. Essentially the same flow features were found for all grid systems, and the 300×200 system is selected for further simulations to resolve the shock wave interactions that may occur in unsteady-state simulations.

Experimental Results and Steady-State Simulation

In Fig. 2, experimental schlieren and OH PLIF images and computational results are compared. In Fig. 2a, the experimental image for the $2H_2 + O_2 + 17N_2$ mixture case, one can see that combustion occurs actively around the wall, especially in the region covered by the expansion wave, impinging shock, and wall boundary. From this experimental result, the viscous effect was supposed to be a major reason for the combustion region formed along the body surface because chemical kinetic calculations show that the ignition delay time behind the postshock region along the forebody is much longer than any other flow timescales.[7] In the $2H_2 + O_2 + 12N_2$ mixture case, shown in Fig. 2b, the combustion region is formed not only around both walls but also along the centerline of the combustor. According to Morris et al.,[7] a small Mach stem is formed at the shock intersection region and results in mixture ignition, even though the flow condition behind the regular intersection of oblique shock waves is not sufficient to induce the combustion just behind the intersection point. From their results, it is understood that there are two combustion mechanisms in ram accelerators: the combustion induced by the viscous effect and the shock-induced combustion. However, the experimental images are not clear enough to support their results, and there could be some questions about the presence and stability of the Mach stem and the significant difference between the two mixtures.

Steady-state numerical analyses were performed to verify the steadiness of the combustion mechanisms of the two experimental cases. All of the flow variables were set initially to the values of inflow in Table 1. Computation is performed with local time stepping with a Courant–Friedrichs–Lewy (CFL) number of 5. Figures 2c and 2d are the resulting overlaid plots of the distribution of the OH mass fraction, temperature contours, and streamlines for each case. The result from the $2H_2 + O_2 + 17N_2$ mixture in Fig. 2c shows the shock trains in the combustor and the combustion region around the wall, and the OH concentration agrees well with the experimental PLIF image. It is also found that the region of high OH concentration matches well with the separated flow region originating from shock wave/boundary-layer interaction. This stagnated flow region is bounded by expansion waves, impinging shock wave, and wall boundary, and the flow temperature increases very greatly beyond the ignition temperature of mixture gas. Thus, the aerodynamic heating in the shock wave/boundary-layer interaction is considered as a major ignition mechanism. Choi et al.[10] have discussed a similar mechanism due to viscous effects in the unsteady-state simulation of a ram accelerator.

The numerical result for the more energetic mixture of $2H_2 + O_2 + 12N_2$ shows that the combustion region also is formed at both walls only. This result is very similar to Fig. 2c, the result for the $2H_2 + O_2 + 17N_2$ mixture, but is significantly different from the experimental result in Fig. 2b. Contrary to the experimental result, there is no combustion region at all along the centerline of the test section, and the Mach stem is not found in the shock intersection region. Although this numerical result corresponds to the theoretical estimation of Morris et al.,[7] that is, the combustion is unlikely to be initiated by the shock heating behind the regular intersection of oblique shock wave, it fails to reproduce the experimental result.[7] To find the cause of this disagreement in the starting unsteady process of the experiment, a more realistic simulation of the experiment was carried out by considering the operation mechanism of the expansion tube.[21]

Initial Condition of the Unsteady-State Simulation and Passage of the Acceleration Gas

Because the steady-state assumption fails to reproduce the experimental result, a more realistic unsteady-state simulation was carried out by considering the passage of the acceleration gas. As an initial condition, it is assumed that the test section is filled with acceleration gas and a normal shock wave passes through the computational domain from the inlet. That is, the postshock condition is applied initially at the inlet. Although helium is used in the experiment, hydrogen is selected as an acceleration gas for

efficiency of the numerical simulation. Because a different acceleration gas is assumed in this study, the initial quiescent condition and the postshock condition of the acceleration gas are calculated from the normal shock theory and contact surface conditions with assumed temperature of 300 K at the initial state. The calculated conditions are given in Table 2. Assumption of hydrogen as an acceleration gas results in a slight overprediction of Mach number and an underprediction of temperature in region 20 in Table 2; it is not significant enough to distort the global flow characteristics.

Because the flow Mach number of the acceleration gas behind the normal shock wave is too small to form an attached oblique shock wave at the body surface, a bow shock will be reflected at the body and the shock wave will move forward to the model front. If a sufficiently long time passes, a bow shock will be formed ahead of the inlet, and this bow shock wave will collide with the contact surface between the acceleration gas and test gas in front of the inlet. Actually, the time needed for the passage of the acceleration gas is about 300 μs (Ref. 22), and this flow collision will occur at the end of the acceleration gas time. Therefore, a considerable distance ahead of the test model should be included in the computational domain to capture this colliding flow. For more precise simulation, the outer flow region of the test model should also be considered to capture the standing bow shock ahead of the model, and the test gas time of about 300 μs should be considered in the simulation. However, the consideration of the outer flow region and the inclusion of this physical acceleration gas time would be a great burden for computations due to the computational time and capacity needed for the simulation of the large physical time and the large computational domain. Therefore, 50 μs of acceleration gas time is assumed, and the effect of the outer flow region is managed as a symmetric boundary condition at a lower and upper boundary ahead of the test model. Although this 50-μs acceleration gas time is small in comparison with the actual value of about 300 μs and the standing bow shock cannot be attained with this boundary condition, the location of the shock wave at 50 μs is considered as having the same order of magnitude as in the actual situation. Also, this assumption is considered as a proper one in regard to the computational load.

The physical time step used in the whole computational process is 7.27 ns, corresponding to a CFL number of 2 for the minimum grid spacing. Because the operating fluid is hydrogen only during the acceleration gas time of 50 μs, the computation was performed excluding the chemistry source term for computational efficiency. After this acceleration gas time, the flow conditions of the mixture at the back of the contact surface were used as inflow boundary conditions, and the computation was performed with the source term of chemical reaction. For the reactive flow simulation, the solution stability needs four subiterations and entropy fixing parameter $\tilde{\varepsilon}$ [Eq. (41) of Ref. 10] of 0.4, even though two subiterations and an entropy fixing parameter of 0.01 seemed to be sufficient for the nonreactive flow calculation of acceleration gas.

Table 2 Deduced flow conditions of the acceleration gas with conditions of the test gas and assumed acceleration gas temperature 300 K

Test gas 5,[a] refraction waves	Acceleration gas	
	20,[a] Contact discontinuity	10,[a] Shock wave
$M_5 = 5.2$	$M_{20} = 1.13$	$M_{S2} = 2.34$
$T_5 = 350$ K	$T_{20} = 596$ K	$T_{10} = 300$ K[b]
$p_5 = 11.2$ kPa	$p_{20} = 11.2$ kPa	$p_{10} = 1.8$ kPa
$u_5 = 2104$ m/s	$u_{20} = 2104$ m/s	$u_{10} = 0$ m/s

[a]Numbers designate flow regions in expansion tube.[21]
[b]Assumed value.

The time-marching progress of the flowfield of acceleration gas is plotted in Fig. 3. Temperature contours are plotted in Fig. 3 for the monotone representation of compressibility and viscosity effects. In Fig. 3, it is shown that typical detached bow shock waves are established by the shock reflection at the upper and lower surfaces as a normal shock rushes into the model ram accelerator. As time passes, two bow shock waves intersect, reflect at the walls, and form a complex intersected shock train. After several times of this intersection/reflection process, a normal shock wave is formed ahead of the test section and runs forward to the inlet. At this stage, the intensity of the shock train becomes very weak, and the gradient of the flowfield is mitigated. Finally at 50 μs, the normal shock moves up to the inflow boundary, and the reactive flow calculation starts from then onwards by applying the postcontact surface mixture condition at the inflow boundary. In addition to the inviscid flow characteristics, we can also see the growth of boundary layers at both walls.

Reactive Flow Simulation for the $2H_2 + O_2 + 12N_2$ Mixture Case

The result of the reactive flow simulation for the $2H_2 + O_2 + 12N_2$ case is plotted in Fig. 4. For the detailed representation of the reactive flow area, the distribution of OH mass fraction is plotted on a logarithmic scale. At $t = 58.17$ μs, just after the beginning of the reactive flow calculation, a fast and weak normal shock wave, a contact surface, and a slow and strong normal shock wave are observed as a result of the intersection between the contact surface and the forward running normal shock wave. As the contact surface and strong normal shock rush into the test section, dual-angled oblique shock waves are formed at the nose of the model ram accelerator. Between the oblique shock waves of different angles, the small angled one is a weak oblique shock wave and the large angled one is a strong shock wave formed by the influence of the high-density region between the strong normal shock wave and contact surface. Mach waves and slip lines are formed at the intersection point. As the time passes, the cross-sectional area of the normal shock wave is getting smaller, and upper and lower strong oblique shock waves intersect with each other at around $t = 80.00$ μs.

The intersection of the strong oblique shock waves forms a new strong normal shock wave or a Mach stem at the center of the test section. Complex wave intersections are noticed during this process, but they do not seem to be important from the viewpoint of major combustion phenomena. The strength of the new Mach stem seems to be greater than the previous normal shock, and the mixture flow ignites by the shock heating behind the Mach stem. After the ignition,

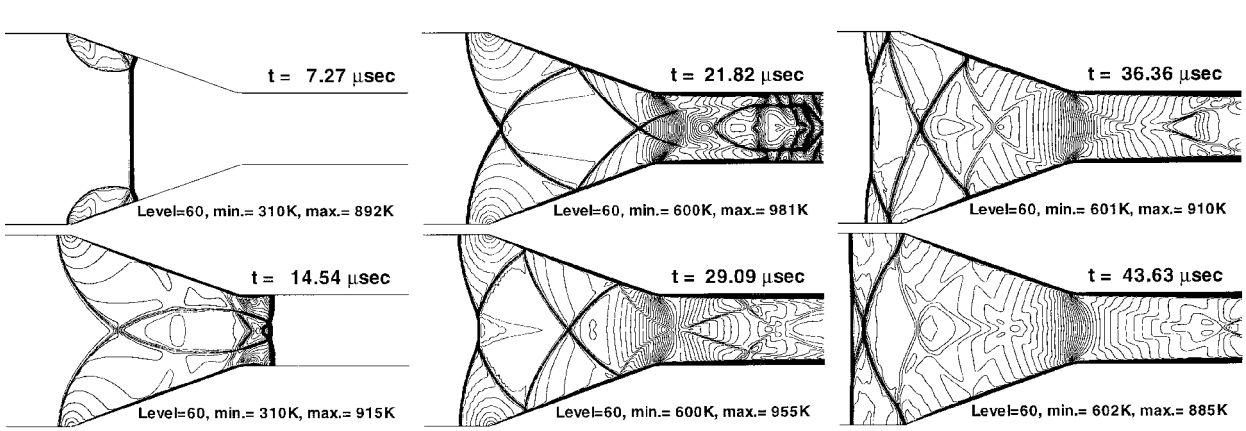

Fig. 3 Resulting temperature contours from the unsteady-state simulation for the acceleration gas; final flowfield data are used as an initial condition for the unsteady-state simulation for the test gas.

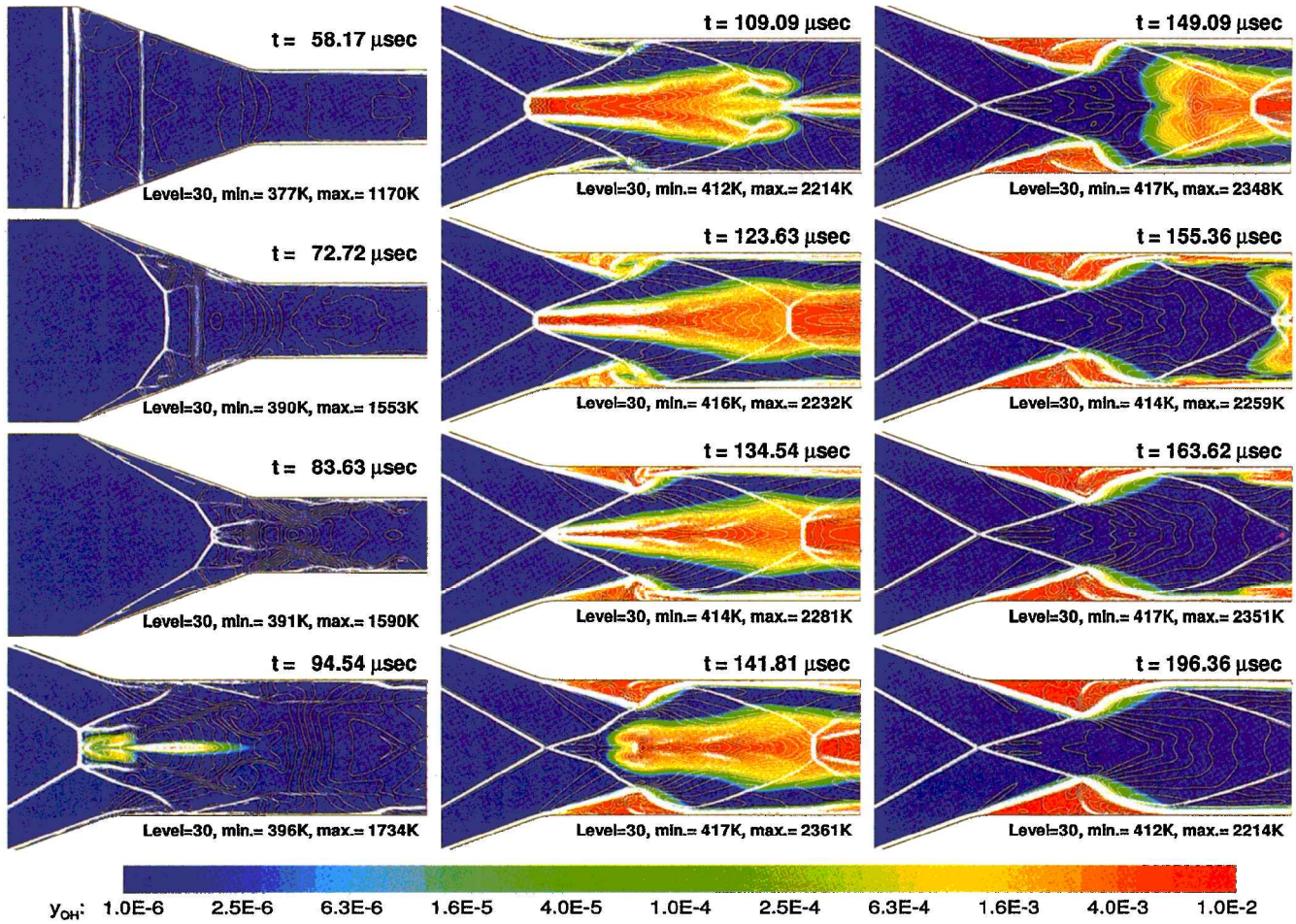

Fig. 4 Overlaid temperature contours and OH mass fraction distributions showing unsteady combustion process of $2H_2 + O_2 + 12N_2$ mixture; combustion region is magnified after $t = 94.54$ μs.

the combustion proceeds very rapidly, and the Mach stem transits to a normal shock-induced combustion or a normal detonation wave. As a result of the presence of a strong normal detonation, the large value of the entropy fixing parameter was needed in the computation, because the small value of it results in carbuncle and even–odd decoupling phenomena. The normal detonation is maintained with a configuration of a triple-point interaction mechanism for a long time after the disappearance of strong oblique shock waves. An oblique shock wave originating from the triple interaction point reflects at the wall surface, and a contact surface (slip line) is formed parallel to the wall, which acts as a flame boundary. The flame boundary is represented as a thick temperature gradient across which the burned gas and the unburned gas are segregated. The combustion initiated by the normal detonation wave forms a long burned gas core that extends to the exit along the centerline of the test section. This transient result is comparable to the experimental result in Fig. 2b. Meanwhile, the intersection of the reflected oblique shock waves makes a secondary Mach stem in the rear part of the test section, which enhances the combustion and forms a secondary combustion zone. This mechanism of shock wave enhancement of combustion is very similar to that of a supersonic diffusion flame.[23]

The burned gas core is maintained for a sufficiently long time as long as the Mach stem (normal detonation wave) exists. However, the cross section of the normal detonation is getting smaller and finally disappears after $t = 134.54$ μs. After the disappearance of the normal detonation, two oblique shock waves intersect with each other at the center of the test section. Behind the regular shock intersection, the flow speed increases to supersonic speed, and the shock heating is not high enough to ignite the mixture. In accordance with the disappearance of the normal detonation wave, the ignition source in the core of test section, the burned gas region detaches at the intersection point of the oblique shock wave and flashes downstream after $t = 138.18$ μs. Therefore, the experimentally obtained schlieren/OH PLIF image of the Fig. 2b case is not considered as an image of stabilized flow but is considered as a intermediate one at a time around 120 μs. Even though the secondary combustion zone enhances the combustion, it is not sufficient to be a flame holding mechanism. Thus, the central burned gas region completely disappears after $t = 163.62$ μs. The flowfield appears to be nearly stabilized after this situation, although there are some disturbances in the boundary layer.

On the other hand, after $t = 95.54$ μs, combustion progresses in the separated flow region that originates from the oblique shock wave/boundary-layer interaction and the adverse pressure gradient. The separated flow region expands with the progress of combustion but is bounded by the tail of the expansion fan, the reflected oblique shock wave, and the wall. The combustion of this separated flow region is ignited by the aerodynamic heating of stagnated flow and is maintained to the end of the computation. Although there could be a question about the structure of vortex in the separated flow region due to the assumption of laminar flow, it would not be an important problem in view of the global combustion mechanism because the separated flow region is bounded by inviscid flow characteristics and does not have a great influence on the global flow features. According to these inviscid and viscous combustion characteristics, the transient solution shows reasonable agreement with the experimental OH PLIF image in Fig. 2b, but the final solution of the unsteady-state simulation agrees with the result of steady-state simulation in Fig. 2d.

Comparison of $2H_2 + O_2 + 12N_2$ and $2H_2 + O_2 + 17N_2$ Mixtures

Unsteady-state simulation of the $2H_2 + O_2 + 17N_2$ mixture case was also carried out to understand the differences of the combustion mechanism between the mixtures. Because the initial condition of acceleration gas is a little bit different from that of the

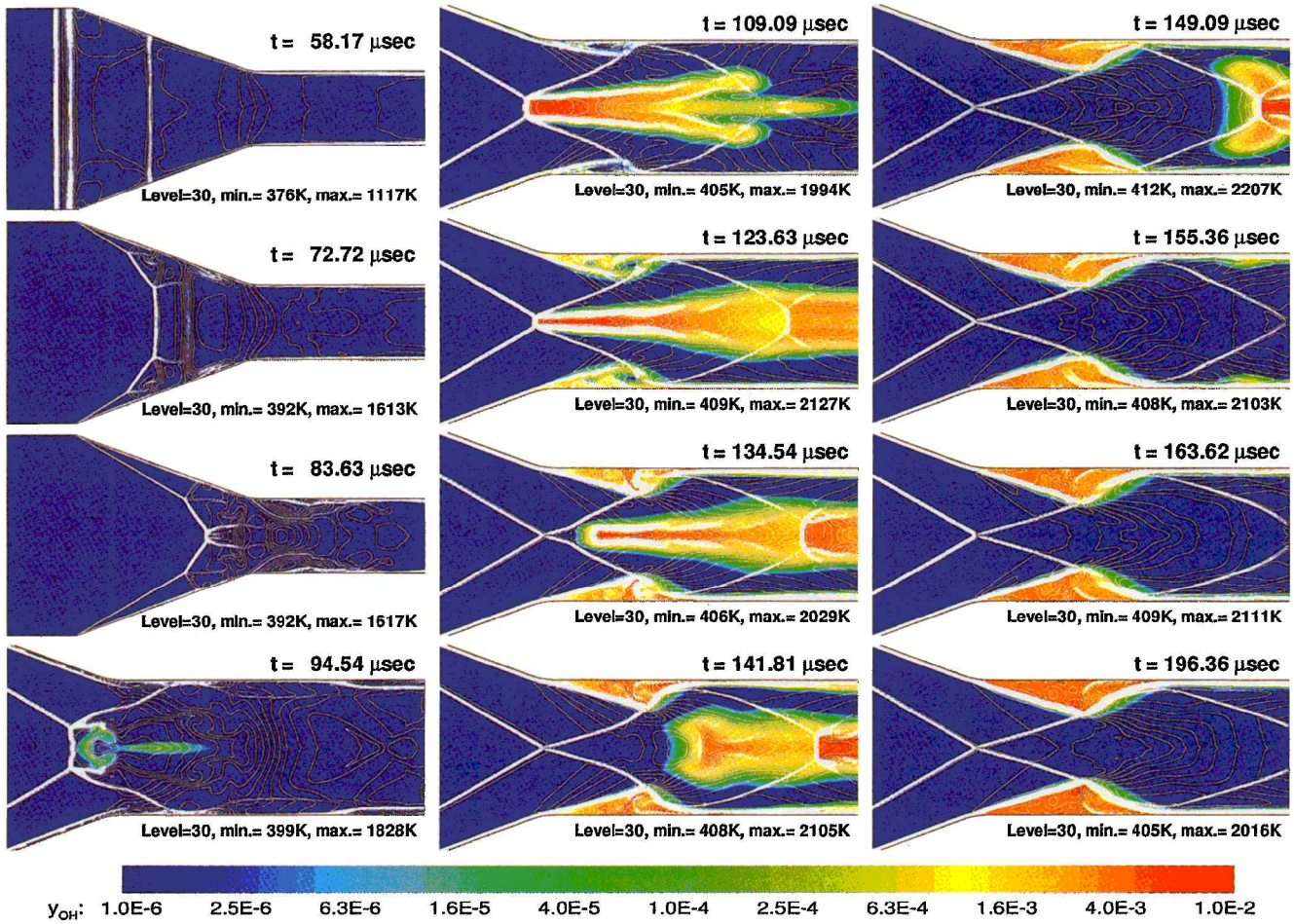

Fig. 5 Overlaid temperature contours and OH mass fraction distributions showing unsteady combustion process of $2H_2 + O_2 + 17N_2$ mixture; combustion region is magnified after $t = 94.54$ μs.

$2H_2 + O_2 + 17N_2$ due only to the slightly different thermodynamic property of the mixture, the same initial condition described in Table 2 is used for this simulation. Thus, the only difference of initial condition is the mixture composition at the inflow boundary, and the difference of the result will only depend on the different sensitivity of the mixture. The time-dependent result of simulation for $2H_2 + O_2 + 17N_2$ mixture case is plotted in Fig. 5.

Because the dilution ratio is the only difference between the cases, the results of unsteady-state simulation show basically the same combustion process as that of the $2H_2 + O_2 + 12N_2$ mixture, as was expected. Combustion occurs along the centerline of the combustor but extinguishes, and the final result is quite similar to the steady-state one in Fig. 2c. The only differences observed at a glance are the late ignition and early extinction. The OH distribution, which is plotted on a logarithmic scale to represent all of the reactive flow region of small OH intensity, makes the distribution look similar to that of the $2H_2 + O_2 + 12N_2$ mixture. However, it is readily understood that the overall level of OH distribution is lower than that of the $2H_2 + O_2 + 12N_2$ mixture by comparing the color level of both cases. If we neglect the green colored area of small OH intensity, the size of combustion regions along the centerline and wall boundary is smaller than that of the $2H_2 + O_2 + 12N_2$ mixture, as shown in the experimental images in Fig. 2.

For the quantitative comparison, the maximum value of the OH mass fraction and the location of the flame front along the combustor centerline are plotted with respect to time in Fig. 6. Along the distribution of the OH mass fraction, we can find that ignition occurs around $t = 90$ μs. After ignition, the OH mass faction is maintained at levels of about 0.01 for the $2H_2 + O_2 + 12N_2$ mixture and 0.006 for $2H_2 + O_2 + 17N_2$. Even though a 40% difference exists between the mixtures, the location of the primary combustion is the same for both cases. Because the combustion zone is sustained aerodynamically by the Mach stem, the combustion zone is maintained for about 30 μs for $2H_2 + O_2 + 17N_2$ and for 40 μs for

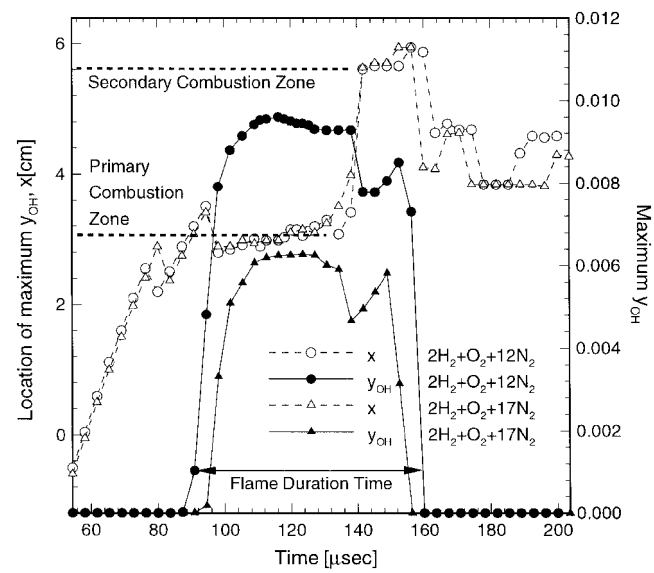

Fig. 6 Maximum value of OH mass fraction and its location along combustor centerline; location x designates the distance from the leading edge of the test section in centimeters.

$2H_2 + O_2 + 12N_2$. Admitting that the heat addition behind the Mach stem could sustain the combustion region for a time, the combustion region finally extinguishes for the present cases. After extinction of the primary combustion zone, the secondary combustion zone has a maximum OH intensity. However, the secondary Mach stem is not strong enough for flame holding, and the combustion zone finally disappears at $t = 160$ μs. The centerline flame duration time is 70 μs for the $2H_2 + O_2 + 12N_2$ mixture and is 60 μs for the

$2H_2 + O_2 + 17N_2$ mixture. In both cases, the overall test time required for flow stabilization is estimated to be about 150 μs, which seems to be a large value in comparison with the 100 ~ 200-μs test time of expansion tube experiments.[22]

Conclusion

Steady- and unsteady-state numerical simulations were carried out to study the ram accelerator flowfield in the expansion tube facility. The present results 1) show reasonable reproduction of the experimental images, 2) present details of the combustion mechanism that are known from the experiment but cannot be proved clearly, and 3) provide solutions to the questions raised by the experimental results.

The combustion region near wall surfaces agrees with the separated flow region originating from shock wave/boundary-layer interaction. The aerodynamic heating in this region is considered as a major ignition source. It is also known from unsteady-state simulation that this viscosity-induced combustion progresses slowly in comparison with the shock-induced combustion along the centerline.

The combustion region along the centerline of the combustor is shown to be a highly transient phenomenon resulting from wave interactions during the developing stage. At an early stage, a Mach stem is formed by the intersection of strong oblique shock waves and ignites the mixture. However, the mixture is not strong enough to make the Mach stem a self-sustaining detonation. Thus, the Mach stem-induced combustion is sustained for a time but finally extinguishes. The flame duration time at the primary combustion zone is about 30 μs for $2H_2 + O_2 + 17N_2$ and 40 μs for $2H_2 + O_2 + 12N_2$. The overall time required for the flow stabilization is about 150 μs, and this value seems to be a long time compared with the test time of the expansion tube experiment. Finally, stabilized flow results are recovered; those are similar to the steady-state result showing only the viscosity-induced combustion region.

Acknowledgments

This study is supported by the Academic Research Promotion Fund for Mechanical Engineering of the Korean Ministry of Education, Grant ME97-G-05. Part of this paper was presented at RAMAC III: The Third International Workshop on Ram Accelerators, Sendai, Japan, July 16–18, 1997.

References

[1]Hertzberg, A., Bruckner, A. P., and Bogdanoff, D. W., "Ram Accelerator: A New Chemical Method for Accelerating Projectiles to Ultrahigh Velocities," *AIAA Journal*, Vol. 26, No. 2, 1988, pp. 195–203.

[2]Bogdanoff, D. W., "Ram Accelerator Direct Space Launch System: New Concepts," *Journal of Propulsion and Power*, Vol. 8, No. 2, 1992, pp. 481–490.

[3]Elvander, J. E., Knowlen, C., and Bruckner, A. P., "High Acceleration Experiment using Multi-Stage Ram Accelerator," *Ram Accelerators*, edited by K. Takayama and A. Sasoh, Springer–Verlag, Heidelberg, Germany, 1998, pp. 55–64.

[4]Knowlen, C., Higgins, A. J., Bruckner, A. P., and Hertzberg, A., "In-Tube Photography of Ram Accelerator Projectiles," *Shock Waves*, edited by R. Brun and L. Z. Dumitrescu, Springer–Verlag, Berlin, 1995, pp. 189–194.

[5]Kruczynski, D. L., Liberatore, F., and Nusca, M. J., "Experimental Flow Visualization for a Large-Scale Ram Accelerator," *Journal of Propulsion and Power*, Vol. 12, No. 1, 1996, pp. 206–210.

[6]Sasoh, A., Hirakata, S., Ujigawa, Y., and Takayama, K., "Operation Tests of 25-mm-Bore Ram Accelerator," AIAA Paper 96-2677, July 1996.

[7]Morris, C. I., Kamel, M. R., and Hanson, R. K., "Expansion Tube Investigation of Ram-Accelerator Projectile Flow Fields," AIAA Paper 96-2680, July 1996.

[8]Yungster, S., "Numerical Study of Shock-Wave/Boundary-Layer Interactions in Premixed Combustible Gases," *AIAA Journal*, Vol. 30, No. 10, 1992, pp. 2379–2387.

[9]Yungster, S., Radhakrishnan, K., and Rabinowitz, M. J., "Reacting Flow Establishment in Ram Accelerators: A Numerical Study," *Journal of Propulsion and Power*, Vol. 14, No. 1, 1998, pp. 10–17.

[10]Choi, J.-Y., Jeung, I.-S., and Yoon, Y., "Numerical Study of Scram Accelerator Starting Characteristics," *AIAA Journal*, Vol. 36, No. 6, 1998, pp. 1029–1038; also AIAA Paper 97-0915, Jan. 1997.

[11]Nusca, M. J., and Kruczynski, D. L., "Reacting Flow Simulation for a Large-Scale Ram Accelerator," *Journal of Propulsion and Power*, Vol. 12, No. 1, 1996, pp. 61–69.

[12]Li, C., Kailasanath, K., and Oran, E. S., "Stability of Projectiles in Thermally Choked Ram Accelerators," *Journal of Propulsion and Power*, Vol. 12, No. 4, 1996, pp. 807–809.

[13]Li, C., Kailasanath, K., and Oran, E. S., "Detonation Structures Generated by Multiple Shocks on Ram-Accelerator Projectiles," *Combustion and Flame*, Vol. 108, No. 1/2, 1997, pp. 173–186.

[14]Jachimowski, C. J., "An Analytical Study of the Hydrogen-Air Reaction Mechanism with Application to Scramjet Combustion," NASA TP-2791, Feb. 1988.

[15]Choi, J.-Y., Jeung, I.-S., and Yoon, Y., "Comparisons of Numerical Methods for the Analysis of Unsteady Shock-Induced Combustion," *Ram Accelerators*, edited by K. Takayama and A. Sasoh, Springer–Verlag, Heidelberg, Germany, 1998, pp. 313–323; also AIAA Paper 98-3217, July 1998.

[16]Roe, P. L., "Approximate Riemann Solvers, Parameter Vectors, and Difference Schemes," *Journal of Computational Physics*, Vol. 43, 1981, pp. 357–372.

[17]Hirsch, C., *Numerical Computation of Internal and External Flows*, Vol. 2, Wiley, New York, 1990, Chaps. 20, 21.

[18]Shuen, S., and Yoon, S., "Numerical Study of Chemically Reacting Flows Using a Lower–Upper Symmetric Successive Overrelaxation Scheme," *AIAA Journal*, Vol. 27, No. 12, 1989, pp. 1752–1760.

[19]Thibault, P. A., Penrose, J. D., Sulmistras A., Murray, S. B., and Labbé, J. L. D. S., "Studies on Detonation Driven Hollow Projectile," *Combustion in High-Speed Flows*, edited by J. Buckmaster, T. L. Jackson, and A. Kumar, Kluwer Academic, Dordrecht, The Netherlands, 1994, pp. 421–446.

[20]Sasoh, A., Higgins, A. J., Knowlen, C., and Bruckner, A. P., "Hollow Projectile Operation in the Ram Accelerator," *Journal of Propulsion and Power*, Vol. 12, No. 6, 1996, pp. 1183–1186.

[21]Trimpi, R. L., "A Preliminary Theoretical Study of Expansion Tube, A New Device for Producing High-Enthalpy Short Duration Hypersonic Gas Flows," NASA TR-R-133, 1962.

[22]Morris, C. I., Kamel, M. R., Stouklov, I. G., and Hanson, R. K., "PLIF Imaging of Supersonic Reactive Flows Around Projectiles in an Expansion Tube," AIAA Paper 96-0855, Jan. 1996.

[23]Huh, H., and Driscoll, J. F., "Shock Wave Enhancement of Mixing and Stability Limits of Hydrogen-Air Flames," *26th Symposium (International) on Combustion*, Combustion Inst., Pittsburgh, PA, 1996, pp. 2925–2932.

K. Kailasanath
Associate Editor

Color reproductions courtesy of Aerospace Propulsion and Combustion Laboratory, Seoul National University.